Radiation-Induced Nanoparticle Formation under Steady-State Radiolysis: Comparison of the Fe, Co and Cr Systems

J.M. Joseph[1], L.M. Alrehaily[1], P.A. Yakabuskie[1], D.A. Guzonas[2] and J.C. Wren[1]

[1] Department of Chemistry, Western University, London, Ontario, Canada N6A 5B7
[2]Atomic Energy of Canada Limited, Chalk River Laboratories, Chalk River, Ontario, Canada, K0J 1J0
(jcwren@uwo.ca)

Abstract

This work involves a comparative study of γ-radiation-induced nanoparticle formation under steady-state irradiation of the Fe, Cr, and Co systems. Water containing initially dissolved metal ions was irradiated in a ^{60}Co γ-cell. The resulting nanoparticles were characterized using FTIR spectroscopy, Raman spectroscopy and XPS. Transmission electron microscopy (TEM) was used to identify the size and shape of the particles. The mechanisms for the formation of γ-FeOOH, Cr_2O_3 and Co_3O_4 nanoparticles are discussed. Depending on the redox potential of the metallic species, either oxidizing or reducing water radiolysis products are responsible for the generation of particle nucleation sites and particle growth. Other key factors that control nanoparticle formation are the pH of the solution and the initial oxygenation of the solution.

1. Introduction

A serious concern for nuclear power plants is materials performance in radiation environments. Corrosion of piping can lead to the release of dissolved metal ions such as iron, cobalt and chromium into the coolant and their transport to the reactor core, either as dissolved ions or suspended particulates (including colloids). These species can be neutron activated and later resuspended into the coolant and deposited outside of the biological shield of the reactor core. There they pose a radiological hazard to the reactor maintenance workers. On-line coolant purification systems are used to remove dissolved ions and particulates, but their removal efficiency depends on the size of the particulates that are present; they are often not effective for removing colloids with sizes less than 0.1 μm.

Water, when exposed to ionizing radiation, decomposes to yield a number of chemically reactive species [1,2]. These water radiolysis products are highly redox active and include both oxidizing (e.g., •OH, H_2O_2 and O_2) and reducing (e.g., •H, $\bullet e_{aq}^-$ and $\bullet O_2^-$) species. These species can readily interact with dissolved metal ions and change their oxidation states. The solubility of a transition metal ion can vary by several orders of magnitude depending on its oxidation state. Therefore, reactions that can alter the oxidation state are important in controlling the concentrations of metal ions in solution and their condensation to form solid particles.

In addition to their importance to nuclear reactor water chemistry and corrosion control, nanostructured transition metal oxides have attracted a lot of attention due to their potential applications. For example, γ-FeOOH has potential application for wastewater treatment to remove heavy metal ions [3]. Chromium oxide nanoparticles have wide application such as green pigments, heterogeneous catalysts, and coating materials for thermal protection and wear resistance [4,5]. Cobalt (Co_3O_4) nanoparticles have been used as high temperature, selective absorbers of solar radiation [6] and anode materials for rechargeable Li ion batteries [7].

Several routes have been used for the synthesis of these transition metal oxide nanoparticles. These include formation of microemulsions, sol-gel syntheses, sonochemical reactions, hydrothermal reactions, and spray pyrolysis [8-10]. Drawbacks of these methods include a low level of control over particle size and composition, and a difficulty in generating a pure, single-phase product. Radiolysis is a promising new technique that addresses these drawbacks. Because γ-radiation penetrates deeply in water, it generates a uniform homogeneous distribution of radiolysis products that, in turn, leads to the simultaneous generation of homogeneously distributed nucleation sites and this leads to the formation of nanoparticles with a narrow, uniform size distribution. Radiation-induced nanoparticle formation is also a cleaner technique since no addition of chemical additives or stabilizers is required for particle formation or size control.

This paper reports on a comparison of the radiation-induced synthesis of γ-FeOOH, Cr_2O_3 and Co_3O_4 nanoparticles from initially dissolved Fe^{II}, Cr^{VI} and Co^{II} ions under steady-state radiolysis condition [11-13].

2. Experimental

High-purity iron (II) sulfate, potassium dichromate and cobalt (II) sulfate obtained from Sigma-Aldrich (purity ≥ 99%) were used to prepare the solutions. All solutions were freshly prepared with water purified using a NANOpure Diamond UV ultrapure water system with a resistivity of 18.2 MΩ·cm. The pHs of the solutions were adjusted using sulfuric acid or sodium hydroxide solutions. The iron (II) sulfate solutions and dichromate solutions were purged with ultra-high-purity argon (Ar) (99.999 % purity) for an hour and then transferred to 20-ml vial (leaving no headspace) inside a glove box under an Ar atmosphere. The cobalt (II) solutions were air saturated by purging with high purity air (Hydrocarbon free) for one hour prior to transfer to a pre-sealed 20-ml vial using a syringe.

The sample vials were irradiated in a ^{60}Co gamma cell (MDS Nordion) as discussed in detail in a previous publication [14]. Following irradiation for a desired period, the samples were analyzed for H_2, dissolved metal ions and particles. The H_2 analysis was performed using a gas chromatograph with a thermal conductivity detector (GC-TCD, 6580 Agilent Technologies) as discussed elsewhere [14].

The colour change in the irradiated solution was monitored by direct UV-VIS measurement and the metal speciation in the solution (both dissolved and dispersed as a colloidal solid) was determined using various colorimetric methods. All of the spectrophotometric measurements were carried out using a diode array detector (BioLogic Science Instruments). The concentrations of Fe^{II} and Fe^{III} species were determined using the ferrozine method as explained in detail in reference [11]. The concentrations of Co^{II} and Co^{III} species (dissolved or dispersed as a colloidal solid) were determined by reacting the sample with 4-(2-pyridylazo) resorcinol (PAR) as described in reference [12]. The diphenyl carbazide colorimetric method was used for determining the Cr^{VI} and Cr^{III} species concentrations as described in reference [13].

Particles were collected from the sample vials by centrifuging the solution and drying the collected solid on a glass plate for Fourier transform infrared spectroscopy (FTIR), Raman and x-ray photoelectron spectroscopy (XPS) analyses. For transmission electron microscopy (TEM) the particles were collected by dipping a carbon-coated copper grid into the irradiated test solution and drying the sample grid in air. The sizes and shapes of the particles were measured using transmission electron microscopy (TEM) with the electron microscope operated at 80 keV. FTIR spectroscopy was performed using a Bruker Vertex 70v, spectra were measured over the 400 to 4000 cm^{-1} range.

3. Results and Discussion

The formation of γ-FeOOH nanoparticles from dissolved ferrous sulfate (section 3.1), Co_3O_4 nanoparticles from dissolved cobalt sulfate (section 3.2) and Cr_2O_3 nanoparticles from dissolved dichromate (section 3.3) were studied using continuous radiolysis [11-13].

3.1 Radiolytic synthesis of γ-FeOOH nanoparticles

Uniform-sized γ-FeOOH nanoparticles were formed by gamma-irradiation of deaerated solutions containing 0.5 mM $FeSO_4$ at pH 5.5, at 6.7 $kGy \cdot h^{-1}$ [11]. The rapid radiolytic oxidation of soluble Fe^{II} to form relatively insoluble Fe^{III} hydroxides leads to particle nucleation by spontaneous condensation.

$$\begin{array}{l} Fe^{II} + \bullet OH \rightarrow Fe^{III} + OH^{-} \qquad (1) \\ \qquad\qquad\qquad\qquad\quad \searrow Fe(OH)_3 \end{array}$$

The primary particles formed by nucleation, insoluble Fe^{III} hydroxide, grow into γ-FeOOH particles that have a dendritic structure. A mechanism that is consistent with this particle evolution was proposed based on the analysis of the aqueous phase and particles.

3.1.1. Aqueous phase analysis

Figure 1a shows pictures of irradiated 0.5 mM Fe^{II} solutions as function of irradiation time. With increasing time the solution changed from colorless to yellow. This is consistent with an increase in the absorption spectral intensity of colloid γ-FeOOH particles at ~ 370 nm as shown in Figure 1b.

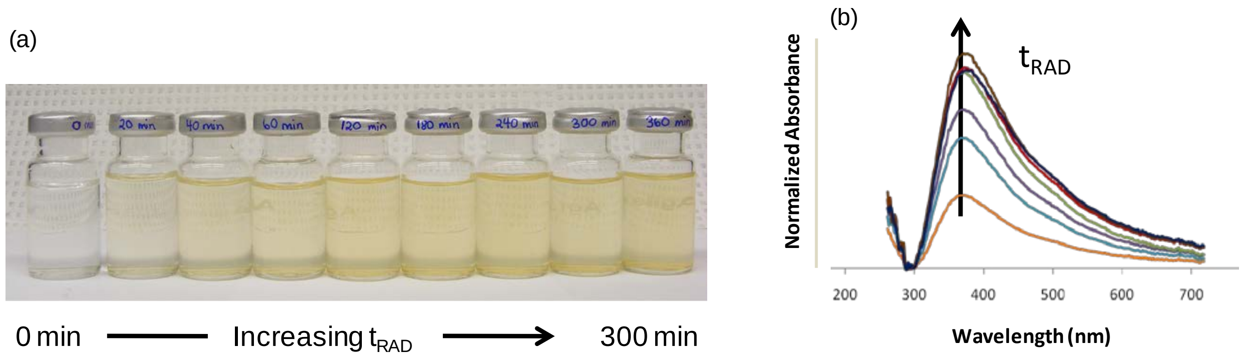

Figure 1: (a) Picture of 0.5 mM $FeSO_4$ solutions as a function of irradiation time. (b) Spectra of the irradiated solutions with the absorption contribution of the hydrated ferric ion removed.

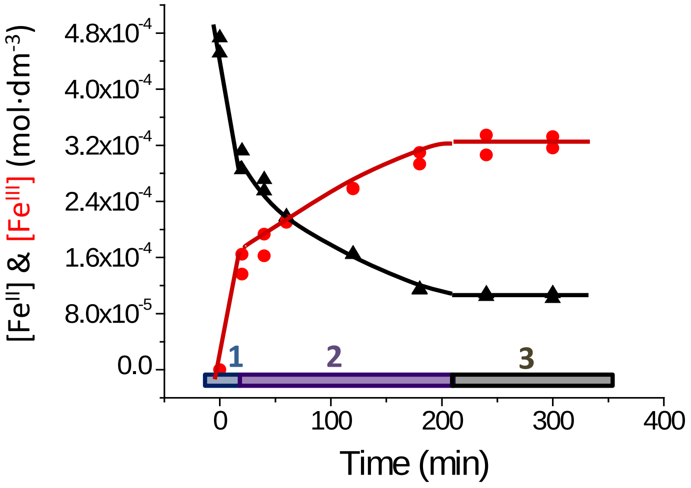

Figure 2: The steady-state concentrations of Fe^{II} (▲) and Fe^{III} (●) as a function of irradiation time for a deaerated 0.5 mM Fe^{II} solution at pH 5.5.

The speciation of Fe^{II} and Fe^{III} as a function of time is shown in Figure 2. Three stages were clearly observed as designated by the horizontal coloured bar and the numbers in the figure. In stage 1 the fast radiolytic oxidation of Fe^{II} to insoluble Fe^{III} occurs, leading to nucleation. Stage 2 involves the growth of the particles; continuing conversion of Fe^{II} to Fe^{III} occurs, but at a slower rate compared to stage 1. In stage 3 the particles grow to their final size and the system reaches steady state. This is consistent with the TEM images shown as a function of irradiation time in Figure 3.

3.1.2. Particle analysis

At short irradiation times (~20 min) spherical particles with a uniform size on the order of 10 nm are observed. Larger particles, approximately 60 nm in size, start to appear at longer irradiation times (≥ 60 min). These larger particles showed a dendritic structure. More prolonged irradiation did not lead to a further increase in the final size of the particles formed or the size distribution. However, longer irradiation did result in an increase in the number of the larger particles formed.

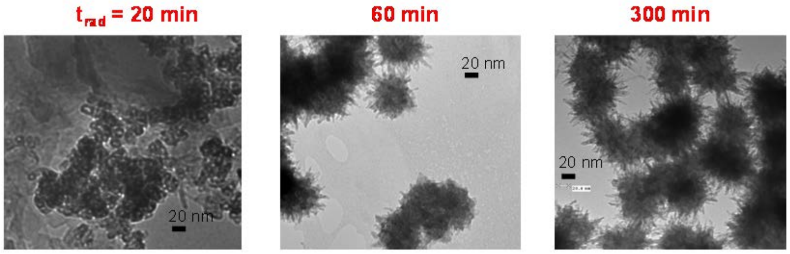

Figure 3: TEM images showing the size and morphology of iron nanoparticles formed by the irradiation of a dearated 0.5 mM Fe^{II} solution at pH 5.5.

The chemical composition and phase of the particles formed were determined using FTIR and Selected area electron diffraction (SAED) as shown in Figure 4. The FTIR spectrum of sample particles is compared with the spectra of standard iron oxides and oxy-hydroxides. The colloidal particle spectrum matches well with that of γ-FeOOH, except for three additional peaks located between 1000 and 1300 cm^{-1}. These peaks are characteristic of S-O stretches and are attributed to terminal SO_4^{2-} groups that adsorbed onto the γ-FeOOH nanoparticle surface. The colloid sample diffraction patterns were found to match the reference line pattern for γ-FeOOH at all locations analyzed, confirming that the composition of the nanoparticles is homogeneous and single phase γ-FeOOH.

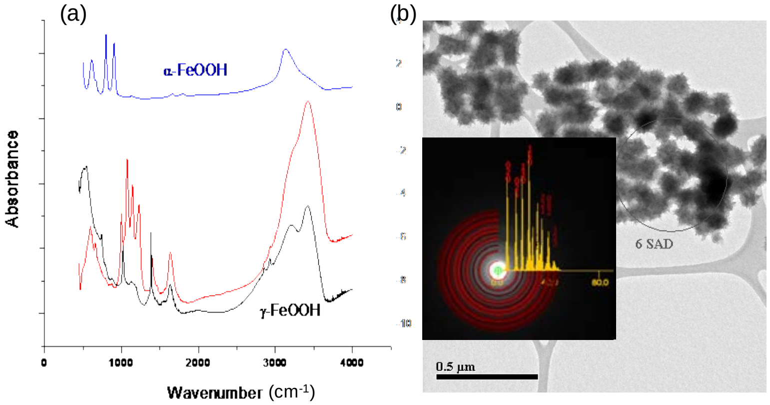

Figure 4: (a) FTIR spectra and (b) the TEM and SAED images of iron nanoparticles formed by the radiolysis of a dearated 0.5mM Fe^{II} solution at pH 5.5.

3.1.3. Mechanism for the radiolytic formation of γ-FeOOH nanoparticles

Figure 5 shows a schematic representation of the proposed mechanism for the formation of γ-FeOOH nanoparticles. The rapid radiolytic oxidation of soluble Fe^{II} to relatively insoluble Fe^{III} hydroxides leads to particle nucleation via spontaneous condensation. This process occurs in stage 1 as evident from Figure 2 and the TEM images (Figure 3). The oxidative power of water radiolysis products (•OH and H_2O_2) is utilized to oxidize the Fe^{II}. In stage 2 the ferrous ions are adsorbed and oxidized on the Fe^{III} nucleates to grow a dendritic structure of γ-FeOOH. The dendritic structure is consistent with the growth of γ-FeOOH crystals by surface oxidation of the adsorbed species rather than homogeneous aggregation of the primary particles. In stage 3 the surface redox reaction rates eventually reach steady state, regulating the further growth of the particles. The rates are related to the surface area available for reaction and this explains the lack of growth of particles beyond a certain size.

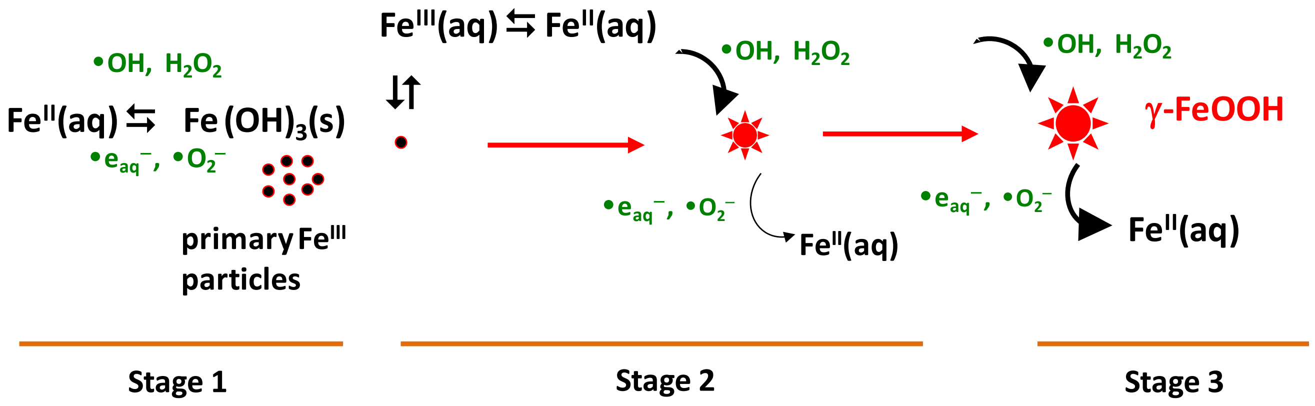

Figure 5: Schematic of the proposed 3 stage growth mechanism of γ-FeOOH particles.

3.2. Radiolytic synthesis of Co_3O_4 nanoparticles

Nanometer sized Co_3O_4 particles were synthesized by the γ-irradiation of aerated $CoSO_4$ solutions at a dose rate of 5.5 $kGy{\cdot}h^{-1}$ [12]. Tests were performed at pH 6.0 and 10.6 with aerated and deaerated 0.2 and 0.3 mM Co^{II} solutions. Nanoparticles were formed only in aerated solutions at pH 10.6. The low solubility of Co^{II} at the higher pH permits condensation of $Co(OH)_2$ particles that act as nucleation sites on which radiolytically-induced heterogeneous oxidation processes can occur. The results show that the particles evolve from $Co(OH)_2$ to CoOOH and then to Co_3O_4 with irradiation time.

3.2.1. Aqueous phase analysis

Figure 6a shows a picture of the irradiated Co^{II} solutions. With irradiation the colour of the pH 10.6 solution changed from light pink to brown, but no colour change was observed at pH 6. The UV-Vis spectra of the test solutions show increases in the intensities of absorption bands with maxima at ~ 280 and 400 nm, Figure 6b. These spectra match very well with a reference spectrum of dispersed Co_3O_4 particles. The good agreement between the reference spectrum and the test solution spectra indicate th at Co_3O_4 is the only coloured species present.

Figure 7 shows that at pH 6.0, the concentration of Co^{II} remains constant, indicating that no oxidation of Co^{II} to Co^{III} occurs even after 5 h of irradiation, consistent with the lack of apparent colour change. At pH 10.6, the Co^{II} is converted to Co^{III} with the reaction reaching completion after about 150 min. The final Co^{III} concentration is less than the initial Co^{II} concentration because some Co is lost from solution in the formation of solid particulates.

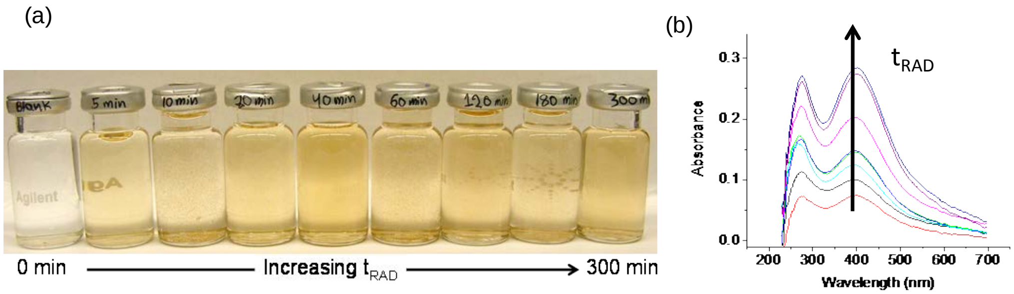

Figure 6: (a) Picture of the irradiated solutions and (b) UV-Vis spectra with background subtracted for aerated 0.3 mM Co^{II} solutions at pH 10.6 and pH 6.0.

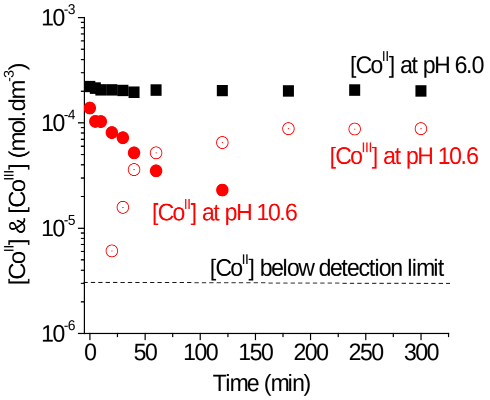

Figure 7: Cobalt speciation as a function of irradiation time for an aerated 0.3 mM Co^{II} solution at pH 10.6 and pH 6.0.

3.2.2. Particle analysis

Figure 8 shows the TEM images of the Co particles formed at pH 10.6 as a function of irradiation time. The TEM images show the presence of two types of particles having very different sizes. The larger particles are ~ 200 nm in width and have a thin hexagonal shape, and these have been identified as $Co(OH)_2$ by XPS (see below). These particles are present in non-irradiated solutions and in irradiated solutions at irradiation times < ~60 min. At longer irradiation times, few of these particles are present. The irradiated test solutions also contain smaller, 8-20 nm spherical particles which have been identified as Co_3O_4 by Raman and XPS. At long irradiation times, the larger particles convert into these smaller particles.

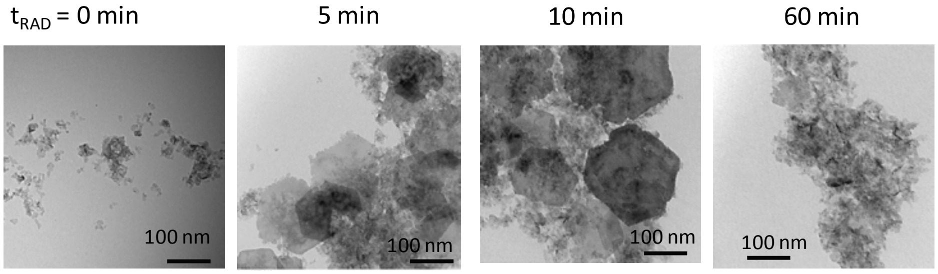

Figure 8: TEM images showing the size and morphology of cobalt nanoparticles formed by the irradiation of an aerated 0.3 mM Co^{II} solution at pH 10.6.

The chemical and phase composition of the particles were determined using Raman spectroscopy and XPS (results shown in figure 9a and b). Comparison of the Raman spectra of the particles with the reference spectra of different Co oxides (Figure 9a) shows that the final particles are composed of only Co_3O_4. The XPS results show that the fraction of $Co(OH)_2$ in the particle decreases with irradiation time while the fraction of Co_3O_4 increases. The fraction of the particle that is an intermediate species, CoOOH, initially increases, reaches a maximum at ~50 min, and then decreases. The particles collected from the solutions irradiated for long times (> 300 min) contain only Co_3O_4.

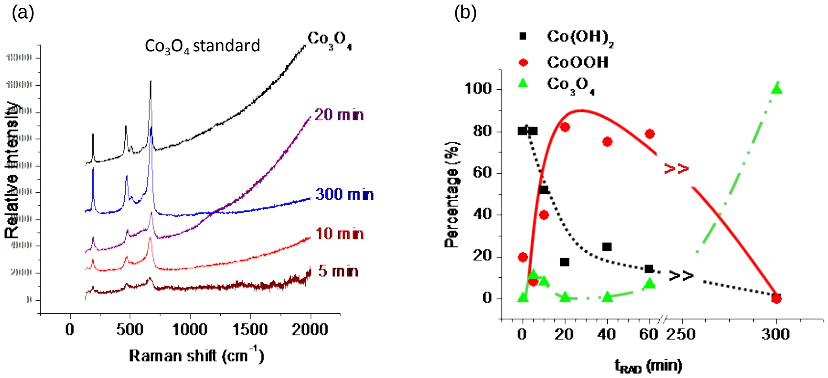

Figure 9: (a) Raman spectra of the particles formed as a function of time along with a spectrum of a Co_3O_4 standard and (b) the percentage of different cobalt species determined using XPS for cobalt nanoparticles formed by the radiolysis of an aerated 0.3 mM Co^{II} solution at pH 10.6.

3.2.3. Mechanism for the radiolytic formation of Co_3O_4 nanoparticles

Figure 10 shows a schematic of the proposed mechanism for the formation of Co_3O_4 nanoparticles under continuous radiolysis. Unlike the Fe system, the homogeneous radiolytic oxidation of dissolved Co^{II} is slow due to the higher oxidation potential for Co^{II}. For cobalt nanoparticle formation, $Co(OH)_2$ particles are formed from hydrolysis of Co^{II} followed by condensation provide nucleation sites for the nanoparticle growth [12]. For this reason, cobalt nanoparticles are not formed at low pHs where the solubility of $Co(OH)_2$ is high. Upon exposure to γ-irradiation, the Co^{II} adsorbed on nucleates will be quickly oxidized to CoOOH by •OH and H_2O_2. The formation of CoOOH stabilizes the nucleation sites since CoOOH is nearly insoluble. The CoOOH then reacts with $Co(OH)_2$ to form Co_3O_4 coupled with the reduction and oxidation of H_2O_2 (Fenton-like reaction).

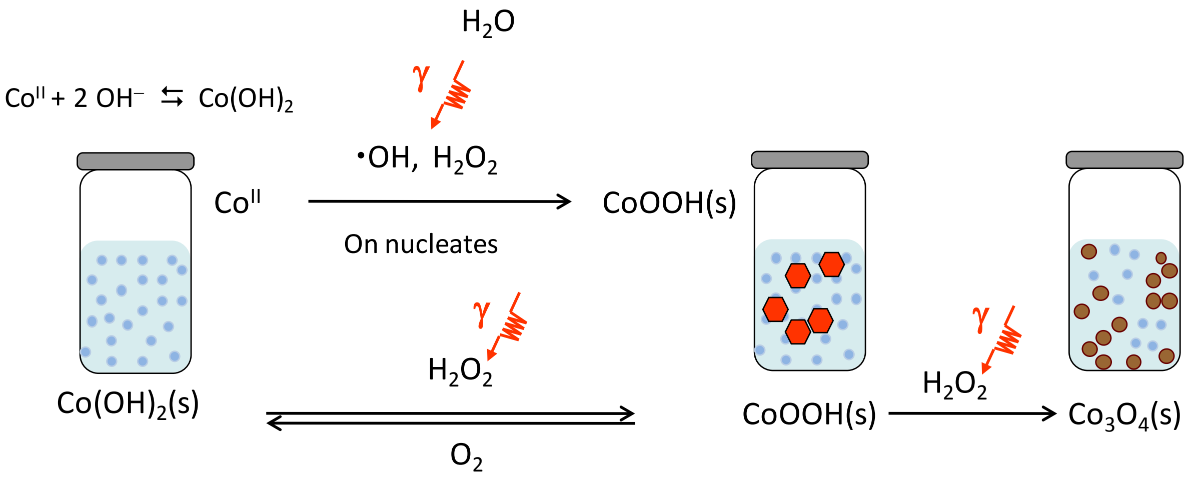

Figure 10: Schematic of the mechanism proposed for radiation-induced cobalt oxide nanoparticle formation.

3.3. Radiolytic synthesis of Cr_2O_3 nanoparticles

Nanoscale chromium (III) oxide particles were synthesized by γ-radiolysis of deaerated Cr^{VI} solutions (CrO_4^{2-} or $Cr_2O_7^{2-}$) at pHs 6.0, 8.5 and 10.6 [13]. No particles were formed in any aerated solution. The reduction of soluble Cr^{VI} to insoluble $Cr(OH)_3$ by the hydrated electron ($•e_{aq}^-$), a powerful reducing agent, leads to the particle formation.

3.3.1. Aqueous phase analysis

Figure 11 shows a picture of deaerated 0.1 mM Cr^{VI} solutions irradiated for different times. The solution colour changes from yellow, characteristic of dissolved $CrO_4^{2-}/Cr_2O_7^{2-}$, to colorless as the irradiation time increases. The colour change is shown more quantitatively by the decrease in the UV-Vis absorption intensity of the solutions at 370 nm (CrO_4^{2-}) with increasing irradiation time.

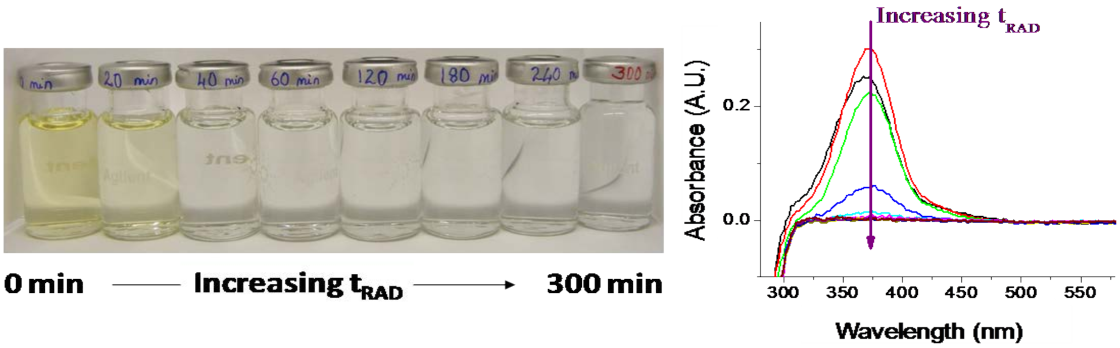

Figure 11: Picture of dearated 0.1 mM Cr^{VI} solutions at pH 8.5 for different irradiation times, and UV-Vis spectra showing the decrease in the intensity of the absorbance peak of Cr^{VI} over the same time period.

The speciation of Cr^{VI} and Cr^{III} in the test solutions is shown in Figure 12 for three different pHs and three solution concentrations. From the figure two stages are clearly observed. In stage 1 there is a fast linear decrease in the Cr^{VI} concentration with time. This is associated with a corresponding linear increase in the concentration of Cr^{III} with time. In stage 2 (after ~30 min) most of the Cr^{VI} has been converted to Cr^{III} and the system trends towards steady state.

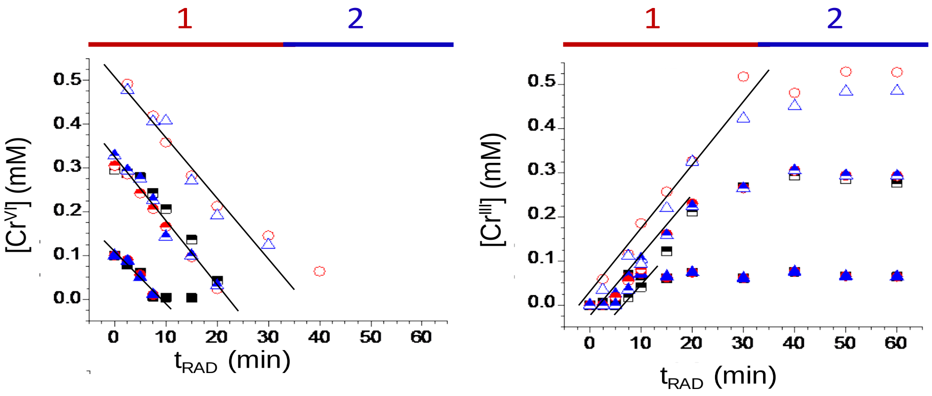

Figure 12: The concentrations of Cr^{VI} and Cr^{III} measured as a function of irradiation time at pHs 6.0 (black, square), 8.5 (blue, triangle), and 10.6 (red, circle) for solutions initially containing a $[Cr^{VI}]$ of 0.1 mM (solid symbols), 0.3 mM (half-filled symbols) and 0.5 mM (open symbols).

3.3.1. Particle analysis

The TEM images of particles formed by the irradiation of 0.1 mM, 0.5 mM and 10 mM Cr^{VI} solutions are shown in Figure 13. The particles are relatively uniform in size, ranging from 9 to 30 nm, and the average size of the particles is nearly independent of pH but increases with chromium concentration.

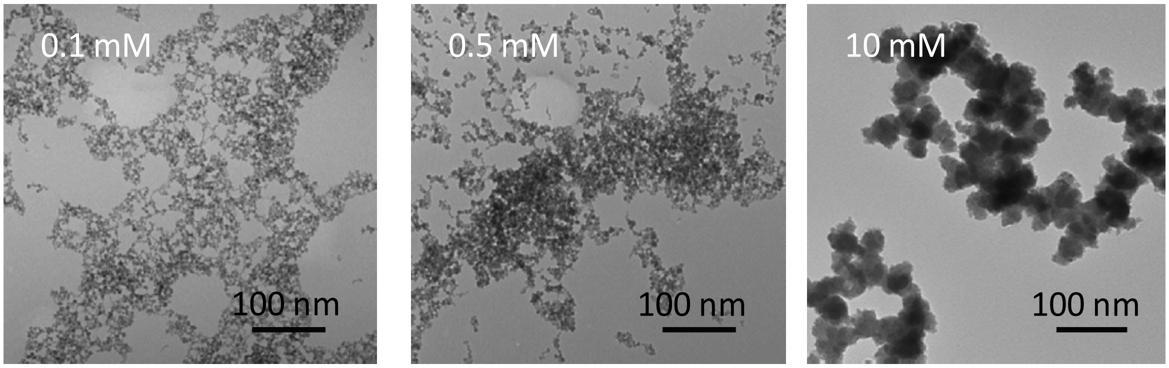

Figure 13: TEM images of chromium oxide nanoparticles formed after 300 min irradiation for 0.1 mM, 0.5 mM and 10 mM Cr^{VI} solution.

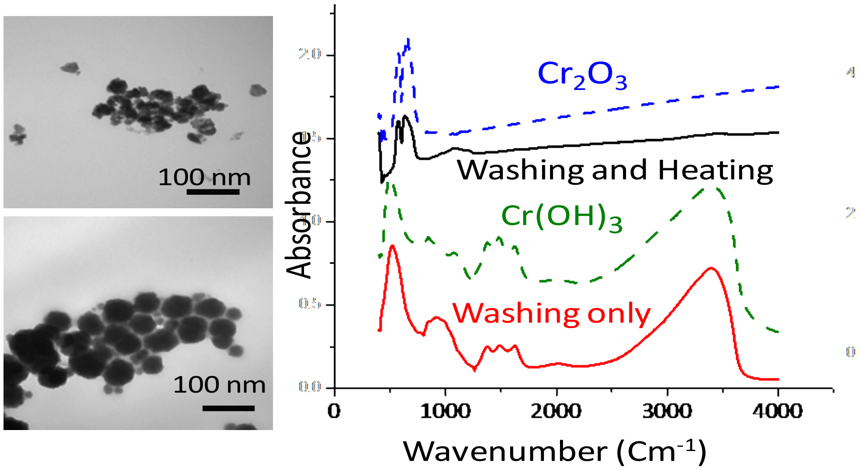

Figure 14: The FTIR spectra and TEM images of chromium oxide nanoparticles after washing and (a) prior to and (b) after heating. Also included are FTIR spectra for Cr_2O_3 and $Cr(OH)_3$.

Figure 14 shows the FTIR spectra and TEM images of collected particles after washing (to remove residual Cr^{VI}) and after drying by heating at 500 °C for 5 h. Figure 14 also includes the reference spectra of Cr_2O_3 (purchased from Alfa Aesar) and $Cr(OH)_3$ (synthesized according to Biesinger *et al*. [15]). The spectrum of the washed particles matches the reference spectrum of $Cr(OH)_3$ while the spectrum of the washed and heated particles matches the reference spectrum of Cr_2O_3. Data obtained by XPS show that the washed particles contain a higher fraction of $Cr(OH)_3$ (72.9%) than Cr_2O_3 (18.5%) while the washed and heated particles are almost pure Cr_2O_3 (98.6%). The heating removes adsorbed water from the particles and converts the $Cr(OH)_3$ to Cr_2O_3.

3.3.3. Mechanism for the radiolytic formation of Cr_2O_3 nanoparticles

A mechanism for the radiation-induced formation of Cr_2O_3 particle is schematically shown in Figure 15. Stage 1 involves the homogeneous aqueous reduction of Cr^{VI} to Cr^{III} by $\bullet e_{aq}^-$. The growth of the particles occur slowly during this phase by agglomeration of $Cr(OH)_3$ that is governed by the Brownian motion. In stage 2, most of the initial Cr^{VI} has been converted to $Cr(OH)_3$ and this continues to condense to form particles. As the $Cr(OH)_3$ particles grow, the interior of the particles dehydrates to form Cr_2O_3 while the outer layer remains hydrated. However, the dehydration rate is very slow since $Cr(OH)_3$ is a relatively stable phase. In stage 2, the redox reactions on the particle surface reach an equilibrium state with both Cr^{III} oxidation by $\bullet OH$ and H_2O_2 and Cr^{VI} reduction by $\bullet e_{aq}^-$ and H_2O_2. The particle size distribution is determined by the steady-state redox conditions at the water-solid interface.

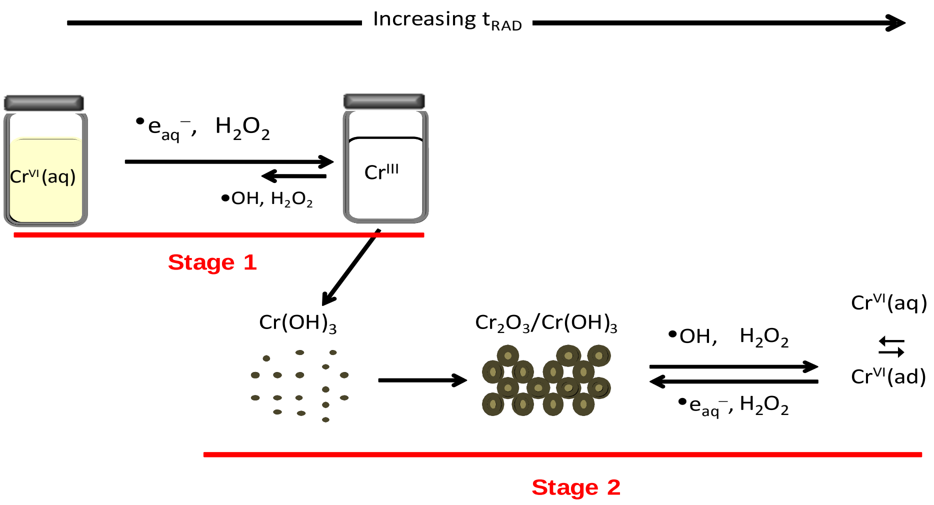

Figure 15: Schematic representation of the proposed mechanism for the radiolytic formation of chromium oxide nanoparticles under steady-state radiolysis.

3.4. Comparison of the iron, cobalt and chromium systems

The iron and cobalt systems behave similarly in the sense that the formation of the metal oxide nanoparticles occurs via a radiolytic oxidation process. The chromium system is very different and the chromium oxide particles are formed by a radiolytic reduction process.

The processes for formation of nanoparticles for the iron and cobalt systems differ in the particle nucleation stage. For iron, particle nucleates are formed by the radiolytic oxidation of Fe^{II} to less soluble $Fe(OH)_3$ which then spontaneously condenses. For cobalt, radiolytic oxidation of dissolved Co^{II} to insoluble Co^{III} oxides/hydroxides is very slow due to the high redox potential of this process. Thus, $Co(OH)_2$ precipitates are required to provide the nucleation sites for radiolytic oxidation to proceed. Once the nucleation sites are available, the particle growth on both Fe and Co systems occur via the same mechanism; Fe^{II} or Co^{II} is adsorbed and oxidized on the particle nucleates to grow into a specific oxide phase, γ-FeOOH or Co_3O_4.

The chromium and the iron systems have similar nucleation processes. For both metals the nucleates formed either by oxidation or reduction of the initially dissolved metal ions are hydrated species, $Cr(OH)_3$ and $Fe(OH)_3$ that do not form coherent solid phases when they condense from supersaturated solutions. However, the rates of formation of the hydroxides are very different for both metals because the $Cr(OH)_3$ can be easily oxidized back to Cr^{VI} by the oxidizing radiolysis products. This slows the net rate of formation of $Cr(OH)_3$. In the iron system, the reduction of Fe^{III} hydrated species by the reducing radiolysis products occurs at a much slower rate compared to the rate or reduction of $Cr(OH)_3$ due to the low reduction potential for Fe^{III} to Fe^{II}. As a result the rate of nucleation by condensation occurs faster in the Fe system.

Even though the solubility of $Cr(OH)_3$ is low, the degree of supersaturation of $Cr(OH)_3$ is lower than in the Fe system because of the back reduction rate and the number of nucleation sites formed is smaller. Because of these thermodynamic and kinetic differences the iron system displays three distinct stages of particle formation: stage 1, nucleation and primary particle formation, stage 2, particle growth into γ-FeOOH in a dendritic structure, and stage 3 where the final sizes of the γ-FeOOH particles are regulated by the steady-state redox conditions established at the aqueous-solid interface of the particles during irradiation. For the chromium system there are only two distinct stages: stage 1, the fast radiolytic reduction of Cr^{VI} to Cr^{III} with slow growth of the particles by the agglomeration of $Cr(OH)_3$ particles, and stage 2 where most of the initial Cr^{VI} has condensed onto the $Cr(OH)_3$ particles and the interior of the particles dehydrates to form Cr_2O_3 while the outer layer remains hydrated.

4. Conclusions

Our study demonstrates that radiolysis of dilute iron, cobalt and chromium solutions can produce highly uniform, nanometer-sized particles depending on the pH and the oxygen content of the solution. The process for particle formation can involve either oxidation or reduction driven by water radiolysis products. The particle formation mechanism depends on the different solubilities of the particular metal oxide/hydroxides and the redox potentials of the metal ions. In all systems, the nanoscale particles that are formed have uniform, narrow size distributions. By understanding the physical and chemical factors controlling particle formation there is a potential to tailor a practical method of synthezising nanoparticles.

5. Acknowledgements

The work described herein was funded under the NSERC (Natural Science and Engineering Research Council of Canada) Discovery grant. The support from the Canada Foundation for Innovation New Opportunity grant and the Ontario Research Fund Excellence in Research: Nuclear Ontario grant are greatly acknowledged for the purchase of the UV-Vis absorption and FTIR spectrometers, respectively. The authors would also like to recognize Dr. Richard Gardiner at the University of Western Ontario Biotron Facility and Dr. Glynis de Silveira and Mr. Fred Pearson at the Canadian Centre for Electron Microscopy, Brockhouse Institute for Materials Research at McMaster University for their assistance with TEM imaging.

6. References

[1] J.W.T. Spinks, R.J. Woods, *An Introduction to Radiation Chemistry*, Wiley, New York, 1990.
[2] J.C. Wren, ACS *Symposium Series*, American Chemical Society, Washington, D.C., 2010, 271.
[3] P. Sabbatini, F. Rossi, G. Thern, A. Marajofsky, M.M. Fidalgo de Cortalezzi, *Desalination*, 251 (2010) 184.
[4] B.M. Abu-Zied, *Appl. Catal. A: Gen*., 198, (2000) 139.
[5] P. Berdhal, *Trans. Am. Soc. Mech. Eng. J. Heat Transfer.*, 117, (1995) 355.
[6] K. Shalini, A.U. Mane, S.A. Shivashankar, M. Rajeswari, S. Choopun, *J. Cryst. Growth.*, 231, (2001) 242.
[7] M.M. Rahman, J.Z. Wang, X-L. Deng, Y. Li, H-K. Liu, *Electrochim. Acta*., 55, (2009) 504.
[8] M. Mohapatra and S. Anand, *International Journal of Engineering, Science and Technology*, 2, (2010) 127.
[9] K. Sinko, G. Szabo, M. Zrinyi, *J. Nanoscience and Nanotechnology*, 1, (2011) 1.
[10] N. Arul Dash, Y. Koltypin, A. Gedanken, *Chem. Mater.*, 9, (1997) 3159.
[11] P.A. Yakabuskie, J.M. Joseph, P. Keech, G.A. Botton, D. Guzanos, J.C. Wren, *Phys. Chem. Chem. Phys*., 13, (2011) 7167.
[12] L.M. Alrehaily, J.M Joseph, M.C. Biesinger, D. Guzonas, J.C. Wren, *Phys. Chem. Chem. Phys.*, 15, (2013) 1014.
[13] L.M. Alrehaily, J.M. Joseph, A.Y. Musa, D.A. Guzonas, J.C. Wren, *Phys. Chem. Chem. Phys.*, 15, (2013) 98.
[14] J.M. Joseph, B.-S. Choi, P.A. Yakabuskie and J.C. Wren, *Radiat. Phys. Chem.*, 77, (2008) 1009.
[15] M.C. Biesinger, B.P. Payne, A.P. Grosvenor, L.W.M. Lau, A.R. Gerson, *Appl. Surf. Sci*., 257, (2011) 2717.